Cronfa - Swansea University Open Access Repository

_____

This is an author produced version of a paper published in:
Corrosion Engineering, Science and Technology

Cronfa URL for this paper:

_____

Paper:

_____

http://www.swansea.ac.uk/library/researchsupport/ris-support/

In-Situ Imaging of Corrosion Processes in Nuclear Fuel Cladding

Alice Laferrere[a][1]*, Robert Burrows*[a]*, Carol Glover*[b]*, Ronald Nuuchin Clark*[b][2]*, Oliver Payton*[c]*, Loren Picco*[c]*, Stacy Moore*[c]*, Geraint Williams*[b]

Corresponding author: Ronald Nuuchin Clark, Ronald.n.clark@nnl.co.uk, 01453 853 601

(a) National Nuclear Laboratory, Building 102B, Stonehouse Park, Sperry Way, Stonehouse, Gloucestershire, GL10 3UT
(b) Materials Research Centre, Swansea University, Bay Campus, Fabian Way, Crymlyn Burrows, Swansea, SA1 8EN, Wales, UK
(c) University of Bristol, Senate House, Tyndall Avenue, Bristol BS8 1TH, UK

Present addresses:
  (1) Atkins, The Hub, Aztec West, 500 Park Ave, Almondsbury, Bristol BS32 4RZ
  (2) National Nuclear Laboratory, Building 102B, Stonehouse Park, Sperry Way, Stonehouse, Gloucestershire, GL10 3UT

Figure captions:

Figure 1: Preparation processes for c-rings.

Figure 2: X-ray diffraction of the surface of the sensitised stainless steel used in the SVET study, prior to metalographic preparation.

Figure 3: Photographic images showing the extent of corrosion on a Magnox alloy specimen, immersed in aerated 2.5% w/v NaCl (aq) at pH 7, for: (a) 3 h, (b) 6.5 h, (c) 8.7 h, (d) 11 h, (e) 16.7 h, and (f) 19 h.

Figure 4: Surface plots showing the distribution of normal current density (jz) above a Magnox alloy specimen, freely corroding in aerated 2.5% w/v NaCl (aq) at pH 7. Scans after: (a) 2 h, (b) 7 h, (c) 10 h, (d) 13 h, (e) 20.5 h, and (f) 22.5 h.

Figure 5: Surface before (a) and at 24 hours (b) immersion at open circuit potential in 1 mol L^{-3} NaCl. (c) montage of the oxide-metal interface following corrosion. Images (d-e) SVET surface current density maps taken after a 3 hour period, with corresponding scale with units are given in (i).

Figure 6: Micrographs of the haematite-metal interface following immersion for 24 hours in 1 mol L^{-3} NaCl in freely corroding conditions.

Figure 7: Mosaic of HS-AFM scans showing microstructure of a thermally sensitised 20Cr-25Ni-Nb stabilised stainless steel specimen (c-ring) cross section.

Figure 8: HS-AFM frames showing grain boundaries in sensitised stainless steel under a droplet of deionised water with 5 mg L^{-1} Cl^{-}: (a) before, and (b) after polarisation. Each 1-megapixel was collected in 0.5 s.

Figure 9: A composite HS-AFM topography map of a Magnox alloy specimen. A filiment of filiform-like corrosion product can be seen passing from left to right. Just to the left of the frame was a large pit with dimensions too deep to image using this technique. The 50 mega-pixel image was collected in 100 s.

In-Situ Imaging of Corrosion Processes in Nuclear Fuel Cladding

Spent nuclear fuel in the UK is stored within ponds dosed with NaOH in order to inhibit corrosion and, to ensure the efficiency of storage regimes, there is a need to define and quantify the corrosion processes involved during immersion of fuel cladding. In this project, state-of-the-art characterisation techniques were employed to image the corroding surfaces of two nuclear fuel cladding materials: stainless steel and Magnox. Advanced gas-cooled reactor (AGR) fuel cladding consists of 20Cr-25Ni-Nb stabilised stainless steel and during irradiation the microstructure of the cladding undergoes significant changes, including grain boundary element depletion and segregation. High-speed atomic force microscopy (HS-AFM) with nanoscale resolution, enabled precipitates and pit initiation in stainless steel to be imaged. Magnox is a magnesium-aluminium alloy and during irradiation in a reactor the outer metal surface oxidises, forming an adherent passive layer which subsequently hydrates when exposed to water. Corrosion processes encompass breakdown of passivity and filiform-like corrosion, both of which were imaged *in-situ* using the scanning vibrating electrode technique (SVET).

Keywords: Nuclear; Filiform corrosion; Intergranular corrosion; Stainless steel; Magnox; Advanced gas-cooled reactor; High-speed atomic force microscopy; Scanning vibrating electrode.

Introduction

In the UK, spent nuclear fuel is stored in ponds awaiting reprocessing or final disposal. Irradiated fuel has been stored for long periods (> 20 years) and there is a need to demonstrate the safety and feasibility of wet storage for at least 80 years. Corrosion of the spent fuel cladding is one limiting factor and tight controls of the pond chemistry are required, since failure in maintaining a high pH or low chloride levels could allow corrosion initiation and compromise the structural integrity of the cladding.

The mechanisms by which spent fuel cladding of light water reactors (LWR) corrodes have been studied in the past [1, 2, 3, 4]. For spent advanced gas-cooled reactor (AGR) fuel, the cladding is made of a niobium stabilised stainless steel and instances of intergranular corrosion (IGC) have been recorded [5, 6, 7, 8, 9]. Novel techniques have been applied to detect corrosion of AGR fuel cladding in the past, such as the use of *in-situ* robotics coupled with ultrasound transducers for 3D scanning to determine wall thicknesses (e.g. post service) [10]. For spent Magnox fuel, the cladding is made of a magnesium-aluminium (Mg-Al) alloy and corrosion sites exhibit dark, filament-like features [11]. The corrosion morphologies of pure Mg have been studied by Williams et al. in the past using *in-situ* scanning vibrating electrode technique [12]. It was found for Mg with an iron (Fe) impurity level of ≤80 ppm, filiform corrosion (FFC) was dominant. Whilst Magnox has a range of alloying additions, the Fe content (≤60 ppm) is similar. Williams et al. [12] proposed that the FFC mechanism is active in this case because relatively low currents were insufficient in sustaining the radial

growth of disc-like corrosion features found on lower purity Mg (≥280 ppm Fe). Corrosion of the Magnox alloy, encapsulated in grout or cements, has also previously been investigated [13].

In this study, corrosion processes in spent fuel cladding are imaged *in-situ* using three different approaches, two of which can be regarded as advanced surface characterisation techniques. High-speed atomic force microscopy (HS-AFM) is a high resolution technique [14] suited for imaging corrosion initiation. This technique is used to study the pit initiation in AGR fuel cladding. The scanning vibrating electrode technique (SVET) is an electrochemical technique and is capable of providing a map of anodic and cathodic activity on the surface of a corroding metal. The SVET is used to analyse IGC on AGR fuel cladding and also the filiform-like corrosion propagation in the Magnox alloy. The Magnox SVET maps are complimented by time-lapse imaging (TLI) which provides detail on the initiation, propagation and extent of FFC.

Investigated Materials

Magnox Alloy

The composition of Magnox alloy is given in Table 1. Each Magnox pellet (16 mm diameter, 3 mm thick) was mounted in a non-conductive resin, with an insulated machine screw inserted to establish the electrical connection.

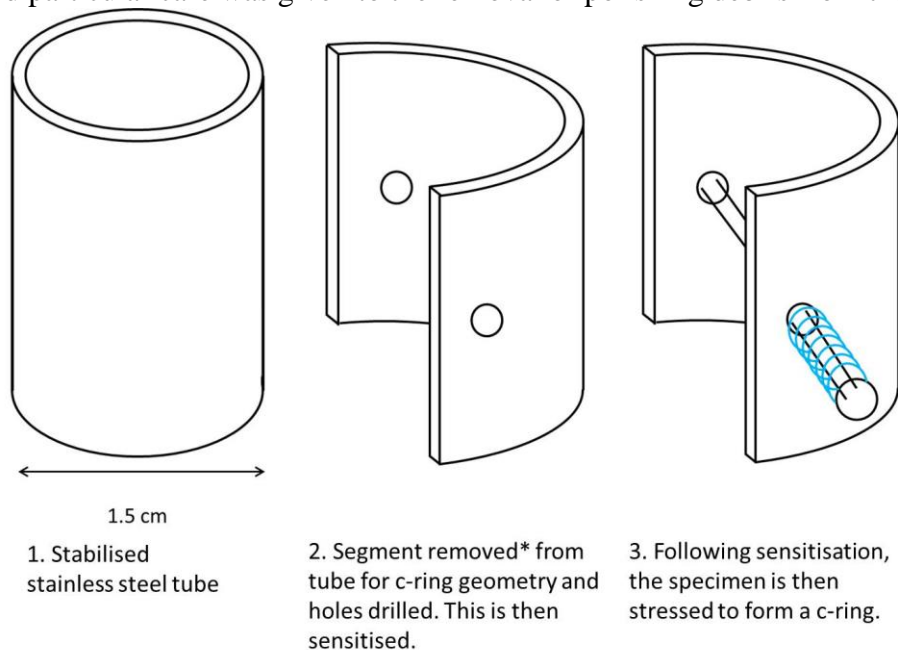Table 1. Magnox composition (transition metals shaded).

Al (wt%)	Be (wt%)	Fe (wt%)	Mn (wt%)	Si (wt%)	Zn (wt%)	Zr (wt%)	Ca (wt%)	Mg
0.70-0.90	0.002-0.03	< 0.006	< 0.015	< 0.01	< 0.01	< 0.01	< 0.008	balance

Specimens were ground with silicon carbide paper and polished using aqueous slurries of 6 μm and a 1 μm diamond paste. Before each experiment, the specimens were thoroughly cleaned and a 1 cm^2 area was delimited with a 90 μm thick extruded PTFE 5490 tape (3M Ltd).

20Cr-25Ni-Nb Stabilised Stainless Steel

During irradiation in a reactor, the stainless steel fuel cladding microstructure may undergo significant changes, referred to as radiation induced segregation (RIS). This is subject to both temperature and radiation dose. Grain boundaries in the 20Cr-25Ni-Nb stabilised stainless steel become depleted in faster diffusing atoms, Cr and Fe, and enriched in slower atoms (Ni). Cr depletion below 12% has been recorded close to grain boundaries in irradiated alloys (up to 200 nm from the grain boundary edge) [5]. To reproduce Cr depletion in un-irradiated cladding, the stainless steel alloys are heat treated and thus become thermally sensitised. During ageing, Cr carbides are formed at grain boundaries and subsequent growth of the carbides depletes in Cr the adjacent region and precipitate-free grain boundaries. In stabilised alloys, such as AGR fuel cladding (where niobium is the stabiliser), not enough carbon is available to form Cr carbides during ageing and a preceding annealing treatment is required to dissolve the niobium carbides present in the as-received alloy and release enough solute atoms.

Offcuts of un-irradiated fuel cladding, made of 20Cr-25Ni-Nb stabilised stainless steel, were cut as C-rings from a tube with a diameter of approximately 1.5 cm. A schematic in Figure shows the processes involved in making the c-rings, following the ASTM standard [15]. C-ring specimens were first annealed for 30 minutes at 1150 °C (followed by quenching in water) and then aged for 50 hours at 600 °C, both steps in flowing argon. Some of the C-rings were mounted in a non-conductive resin and an electrical connection was established on the curved side of the C-ring, with a bolted connection to a PTFE insulated wire. The cross sections (perpendicular to the extrusion direction) were prepared according to Warren et al. [15]. The quality of the surface finish is crucial in obtaining high resolution HS-AFM scans and particular care was given to the removal of polishing debris from the scratch-free surface.

1.5 cm

1. Stabilised stainless steel tube

2. Segment removed* from tube for c-ring geometry and holes drilled. This is then sensitised.

3. Following sensitisation, the specimen is then stressed to form a c-ring.

*In this schematic half of the tube has been removed for the c-ring geometry for simplification. In practice a smaller segment is removed.

Figure 1: Preparation processes for c-rings.

Specimens prepared for SVET were of the same stainless steel grade, but supplied from Springfields Fuels Ltd. as flat plate ~0.8 mm thick. The specimen prepared for SVET was annealed at 1150 °C for 30 minutes under argon, quenched in water, and then aged at 600 °C for 336 hours in air. Following the thermal treatment, a dark coloured scale was present over the material, which was determined to be an iron oxide (haematite (Fe_2O_3)) using X-ray diffraction (Figure 2). The plate was cut into a ~2 cm square and mounted in a non-conductive cold set resin. The specimen surface was prepared by grinding, then polishing using water-based 6 μm colloidal diamond, and subsequently 1 μm solution. The grinding was conducted at an offset angle to investigate the influence of sensitisation as a function of depth [7], as previous (unpublished) results indicated that the stainless steel may not have been sensitised through the thickness of the material. The specimen was prepared following the same procedure as is described in [7].
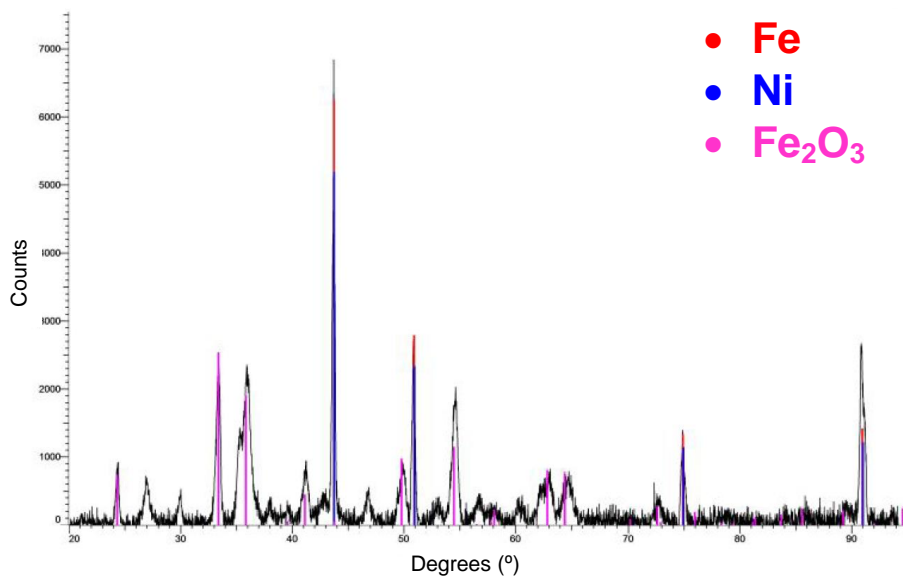
Figure 2: X-ray diffraction of the surface of the sensitised stainless steel used in the SVET study, prior to metalographic preparation.

Scanning Vibrating Electrode Technique

In the early years of spent fuel storage, instances of corrosion have been recorded in irradiated Magnox fuel cladding. To prevent corrosion of the Magnox alloy, the levels of chloride in ponds are kept to a minimum (<0.5 ppm) and the ponds are dosed to pH 13 [16]. AGR fuel cladding is also pond stored in a low chloride environment (<0.5 ppm in enclosed ponds) and also dosed with sodium hydroxide (≈pH 11.4) [16].

The mechanism by which Magnox alloy corrodes in an aggressive environment is not fully understood. In previous papers [12, 17], the SVET has successfully been applied to elucidate corrosion mechanisms by imaging electrochemically active regions during corrosion propagation in Mg and Mg alloy. In this work, freshly polished surfaces of Magnox alloy were imaged with the SVET and corrosion was accelerated by choosing an electrolyte with a high concentration of aggressive anions (2.5% w/v NaCl) compared with the pondwater.

Technical Background

SVET is an *in-situ* technique measuring the potential gradients induced by the ionic current flow above an electrochemically active surface. The gradients are measured at specific points by vibrating a fine tipped microelectrode 100 μm above the specimen surface. The active portion of the probe tip consists of a 125 μm diameter platinum micro-disc electrode and the total tip diameter is ≈ 250 μm [18]. A large area (2.5 x 2.5 cm), low impedance silver chloride reference electrode, located ≈ 5 cm from the vibrating probe, acts as an instrument earth. After calibration of the instrument in the same electrolyte as the electrolyte chosen for the experiment, the peak-to-peak SVET voltage signal was converted to a current flux density along the axis of probe vibration, j_z. Further information on the details of the instrument design and calibration can be found elsewhere [18, 19].

The specimen was fully immersed in ≈ 3 litres of unstirred electrolyte. By scanning the vibrating electrode over a fixed area, a map of current density can be obtained for the corroding surface. For the Magnox experiment, scans were taken every 12 minutes for a period of up to 48 hours. Scans were taken at 3 hour intervals for the 20Cr-25Ni-Nb

experiment. The stacking of the different maps taken at a fixed interval reveals crucial information about the spatial evolution of localised cathodic and anodic areas. Thanks to this new technique, the corrosion propagation mechanism can be elucidated.

Results

As soon as the Magnox alloy was immersed in 2.5% w/v NaCl at neutral pH, large hydrogen bubbles appeared on the polished surface. Those bubbles later coalesced and migrated to the side of the studied area. To record the evolution of corrosion features on the surface TLI was employed. A high quality photograph was taken every 30 seconds with a computer-controlled Nikon D70S digital SLR camera fitted with an AF-micro close-up lens. Corrosion initiated after 3 hours of immersion. **Figure 3**(a) shows that the initiation site is far from the edges of the studied area, indicating that the PTFE tape had no effect on corrosion initiation.
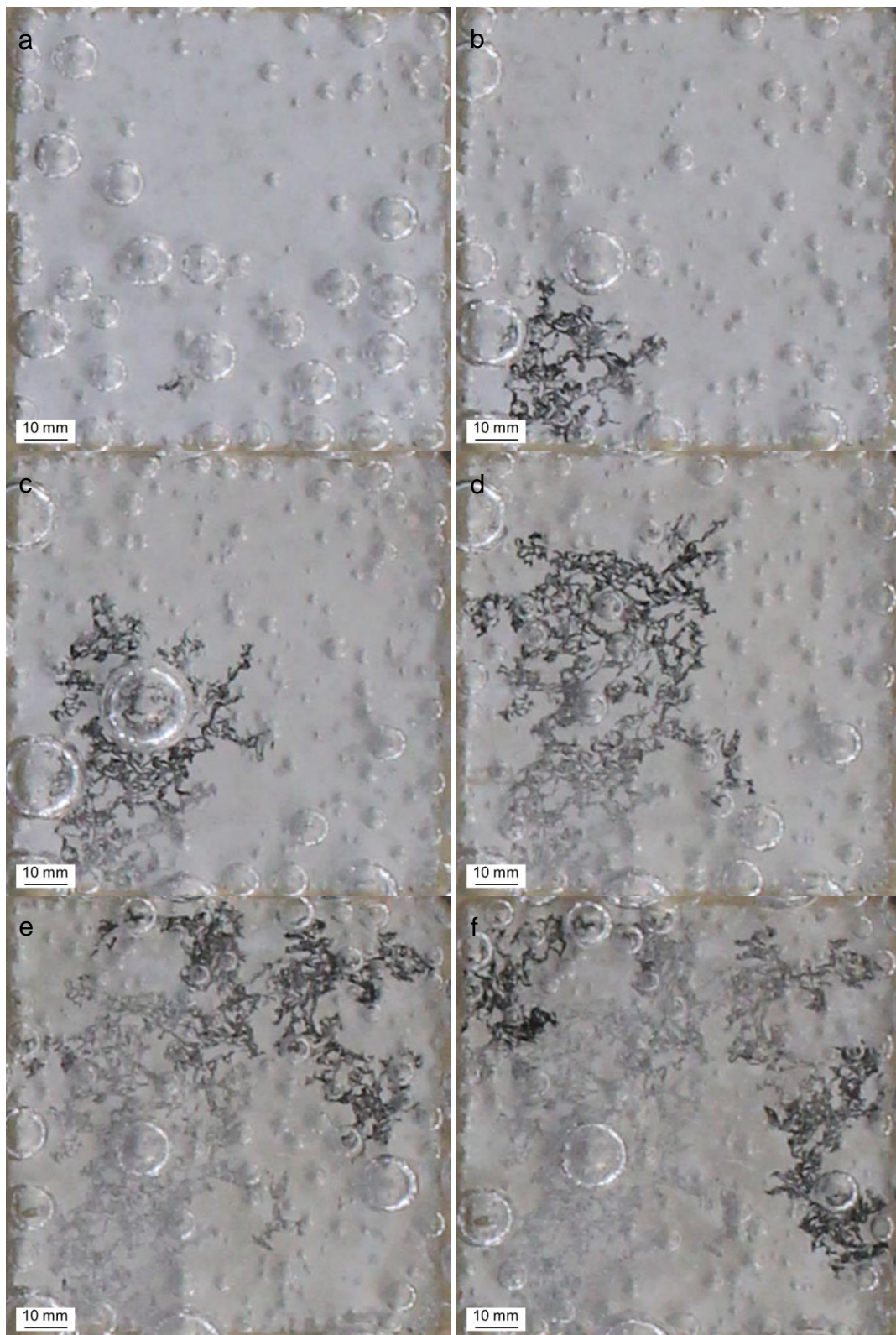
Figure 3: Photographic images showing the extent of corrosion on a Magnox alloy specimen, immersed in aerated 2.5% w/v NaCl (aq) at pH 7, for: (a) 3 h, (b) 6.5 h, (c) 8.7 h, (d) 11 h, (e) 16.7 h, and (f) 19 h.

Active areas, where metal has been dissolved, appear as black filaments. At the head of the filament, intense and continuous hydrogen bubbling was recorded. The filament head then propagated to the surrounding region, leaving a narrow dark track on the surface, before splitting up into several propagating tracks. At the leading edge of each filament, a stream of hydrogen bubbles emanated. Previous work by Williams [18, 20, 21] has shown that the head

of the filiform is a highly-focussed net anode. This anode then propagates, leaving behind net cathodic areas as 'tracks'. The forward motion of the filiform is driven by the previously attacked cathodic regions where hydrogen evolution occurs. Further details on this mechanism can be found in [12].

After 8 hours of immersion, black filaments that were active in the early stage of corrosion propagation, appear as dark grey filaments (**Figure 3** (c) to (e)). This change of morphology only affects thread-like tracks far away from the active filament head and is likely to correspond to the hydration of the corrosion product, initially formed as a dense oxide/hydroxide duplex film into a porous highly hydrated hydroxide, according to the reaction:

$$MgO + H_2O \rightarrow Mg(OH)_2$$
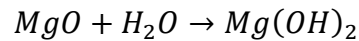
The active region of the black track repassivated quickly once the filament head propagated to the surrounding area. The corrosion front spread from the bottom left hand corner (**Figure 3** (b)), to the top left and then top right corner (**Figure 3** (d) and (e)), to finally dissolve metal in the bottom right corner (**Figure 3** (f)). After 20 hours of immersion, the entirety of the initially polished surface has corroded and most of the previously black filaments turned into grey filaments, a change thought to correspond to the hydration of corrosion product.

A different specimen with a similar surface finish and immersed in an electrolyte with the same chemical composition was studied with the SVET. A data point was taken every 200 μm and the area scanned was 8 mm x 8 mm. Positive current densities (anodes) are shown in red, and negative current densities (cathodes) are in blue. As soon as the specimen was immersed in 2.5% w/v NaCl at neutral pH, the surface was covered with large hydrogen bubbles. Localised anodic activities (≈ 7 A.m^{-2}) were recorded after one hour of immersion and in every successive scan for two hours. The first anodic peak was at the edge of the scanned surface and grew slightly larger before splitting in multiple anodic peaks (**Figure 4** (a)). There were no cathodic peaks in the vicinity of the anodes, and only one data point, more than 5 mm away from the corrosion activity, was recorded as slightly more cathodic than its surroundings. This point is most likely a spurious data point, probably due to the presence of an impurity on the surface.

After 7 hours of immersion, strong anodic activity was recorded at the opposite edge of the scan area (**Figure 4** (b)). Again, this strong anodic peak divided into several peaks of similar amplitude and a slight cathodic activity was recorded in the peaks surroundings (indicated by an arrow in **Figure 4**(c). In previous scans, a strong anodic peak was recorded at the location of this small cathode. This result corroborates with the propagation of black filaments recorded with TLI (**Figure 3**), where the leading edges of the dark tracks are regions of intense anodic activity which quickly passivate as the anodic peaks move away from their point of initiation and leave behind regions of cathodic activity.

The anodes then propagated over the surface (**Figure 4**(c) and (d)) and split into several weaker anodes (**Figure 4** (e) and (f)). The anodic peaks were located at the head of a black thread-like filament evident on the corroding surface, where intense hydrogen bubbling was also recorded. After 20 hours of immersion, the hydrogen bubbles were scarcer and numerous small cathodes were evident close to the anodic peaks. However, previous studies on FFC in magnesium alloys [12] reported stronger cathodic activity behind the leading edge of the dark filament. Also the cathodic sites themselves do not appear to be strongly-linked to the anodic activity spatially i.e. the anodic "front" appears to be at a distance away (> 1 mm) from the

most dominant cathodic sites. In this study of corroding Magnox alloys, the lack of clear cathodic activity in the SVET scans could be because:

- The cathodes and anodes are not separated by >100 µm, the spatial resolution of the SVET probe.
- And/or hydrogen bubbles are interfering with the probe and higher current densities are measured. Indeed, bubbles are expected to increase the resistivity of the SVET probe. This explains the presence of small cathodic activity recorded by the SVET probe in the later stages of corrosion propagation, when fewer hydrogen bubbles were noticed.

The anodic peaks recorded were at the head of dark filaments, similar to filaments photographed in the TLI experiment. Once the anodic region is passivated, the anode "switched off" and the corrosion front spread to the surrounding region. Hence, the anodic peaks recorded with the SVET were seen as propagating over the surface. The proximity with a cathode (less than 100 µm), where hydrogen evolution takes place, will decrease the pH and passivate the anodic region. This could be linked with the evolution of the corrosion product morphology noticed during TLI, where the filament colour changed from black to grey.
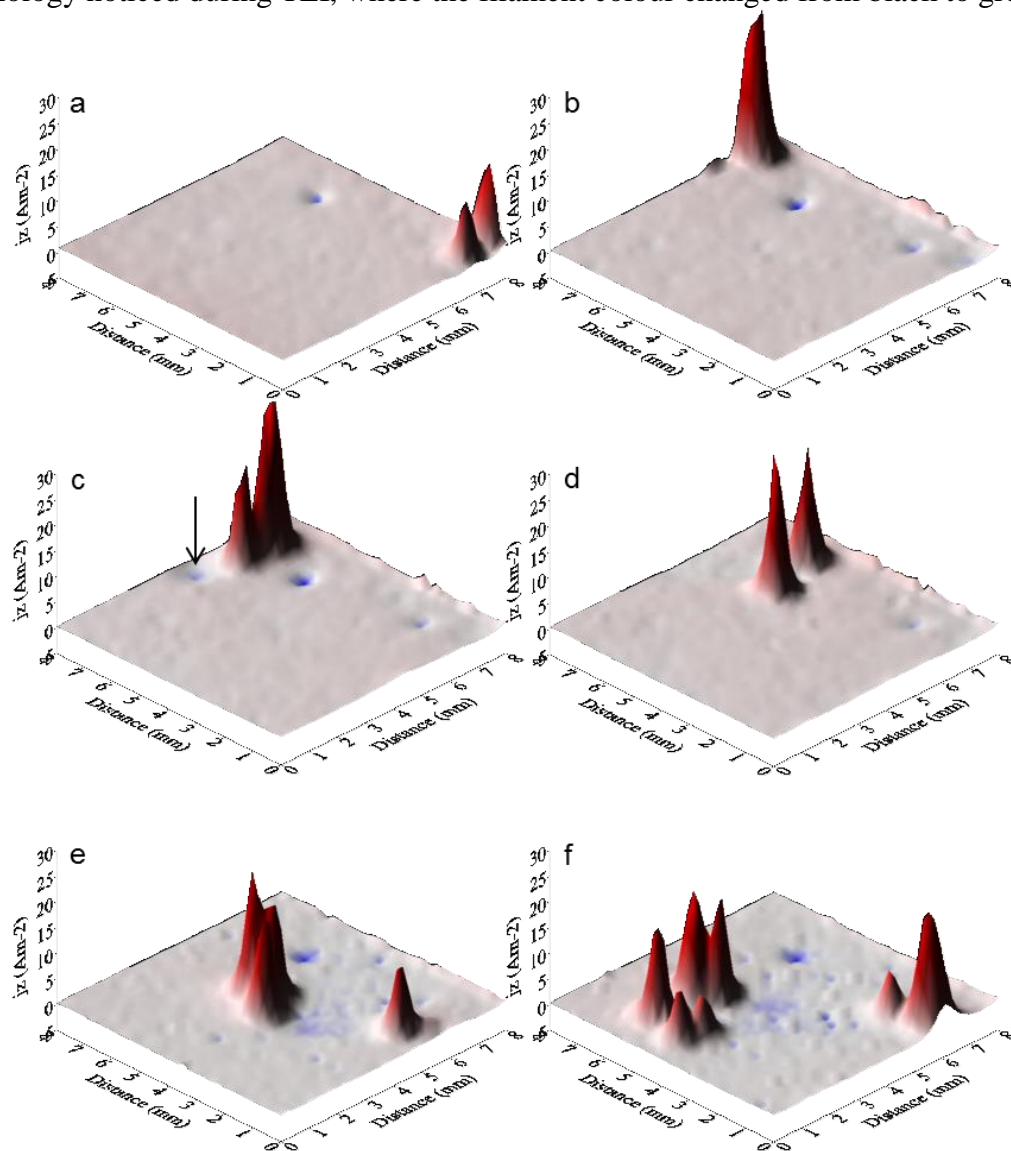

Figure 4: Surface plots showing the distribution of normal current density (jz) above a Magnox alloy specimen, freely corroding in aerated 2.5% w/v NaCl (aq) at pH 7. Scans after: (a) 2 h, (b) 7 h, (c) 10 h, (d) 13 h, (e) 20.5 h, and (f) 22.5 h.

Figure 5(a, b, c) show the extent of corrosion on the sensitised stainless steel surface, which corresponds to the surface current density maps shown (d-h). The top left of the surface **Figure 5**(a, b) is due to the grinding offset applied, determined using X-ray diffraction as Fe_2O_3. Within 3 hours of immersion in 1 mol L^{-3} NaCl corrosion had initiated at the Fe_2O_3-metal interface, the region thought to be most heavily sensitised. The image in (b) correlates to the SVET maps in (f-g) which indicates that corrosion propagated under the Fe_2O_3 where sensitisation was greatest, but also where there was occlusion of oxygen. It is postulated that this formed a differential aeration cell, leading to false probe readings for the scans shown in **Figure 5**(e, f, g). There exists the possibility that the crevice environment may have been disturbed (e.g. removal of perforated Fe_2O_3 iron oxide) in (h), leading to a different probe reading.

The extent of IGC can be seen in **Figure 6**(a) which shows the area in which the differential aeration cell developed. The micrograph in **Figure 6**(b) shows the extent of IGC and intergranular pitting which occured at select grain boundaries. Note the width of IGC at the grain boundaries decreases further away from the haematite-metal scale.
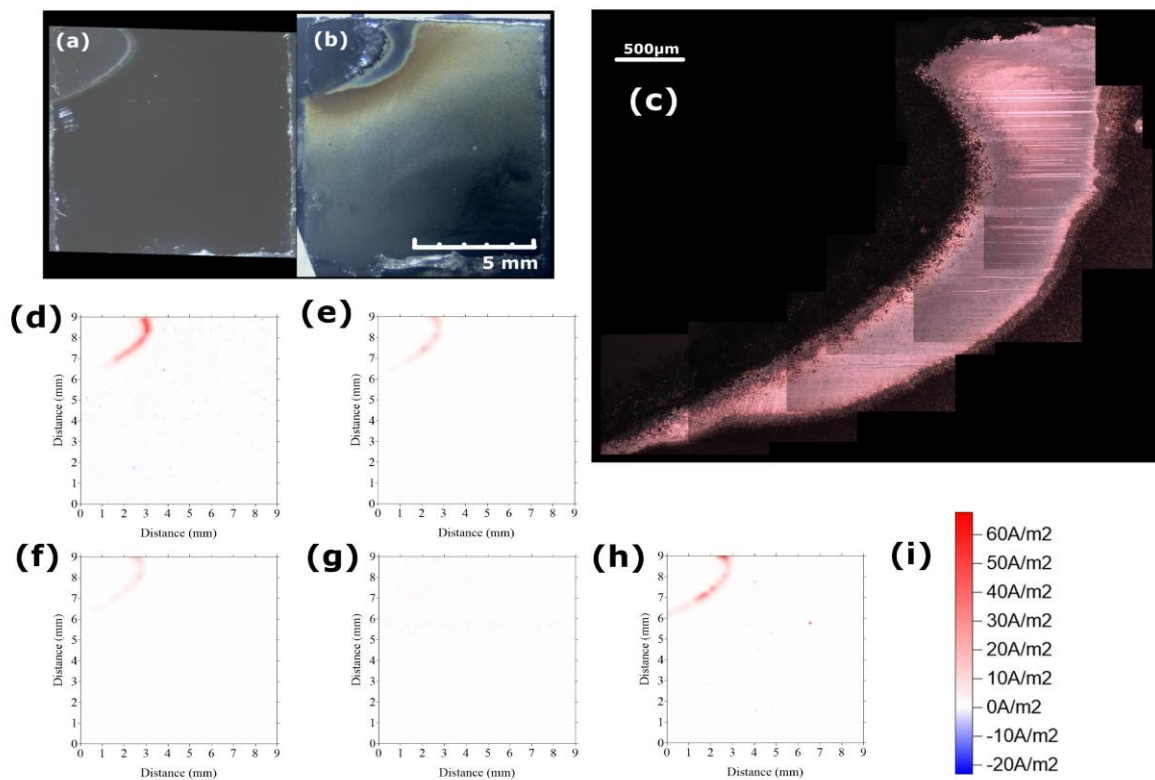

Figure 5: Surface before (a) and at 24 hours (b) immersion at open circuit potential in 1 mol L^{-3} NaCl. (c) montage of the oxide-metal interface following corrosion. Images (d-e) SVET surface current density maps taken after a 3 hour period, with corresponding scale 80 to -20 Am^{-2} with units are given in (i).
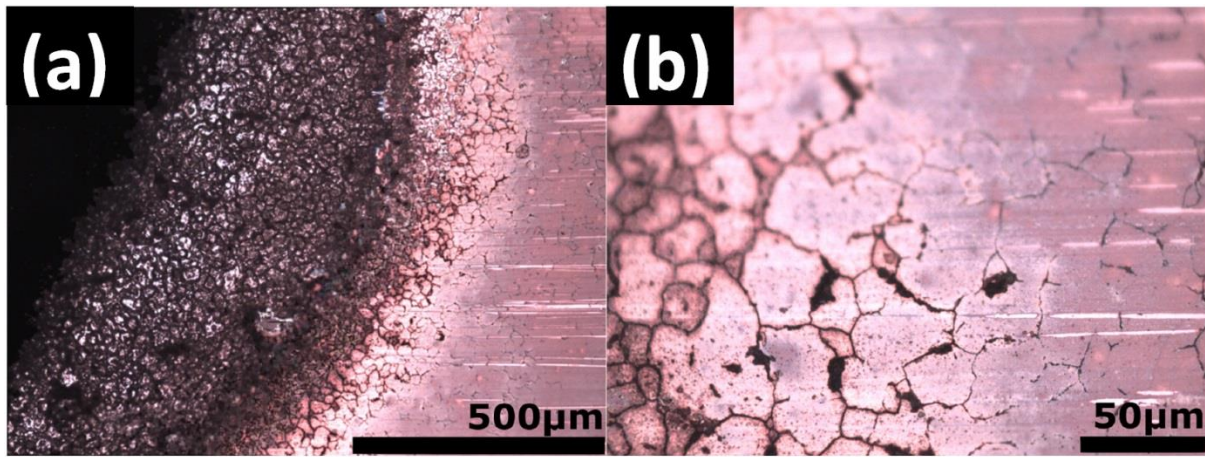
Figure 6: Micrographs of the haematite-metal interface following immersion for 24 hours in 1 mol L^{-3} NaCl in freely corroding conditions.

High-speed Atomic Force Microscopy

Spent AGR fuel cladding has been successfully stored in spent fuel ponds since 1988 [17] using NaOH as a corrosion inhibitor. However under different parameters IGC may initiate i.e. if reactor sensitised AGR fuel cladding was present in abnormally high chloride pond chemistry without an inhibitor. An experiment was designed to image the first stages of corrosion in a replica alloy to understand the role of carbides in corrosion initiation. Cross sections of thermally sensitised stainless steels were scanned with a custom-built HS-AFM in an aqueous environment at a high pixel rate providing two megapixel images per second of a 4 x 4 μm area. The nanometre lateral and sub-atomic height resolution enables the clear visualisation of carbides at grain boundaries, which are only hundreds of nanometres wide. Corrosion was initiated by polarising the specimen in a chloride environment.

In addition, the Magnox alloy specimen was imaged post-corrosion, allowing for further analysis of the black filament structures on the surface.

Technical Background

An atomic force microscope (AFM) maps the topography of the specimen by raster-scanning the surface with an extremely sharp tip on the end of a micro-cantilever beam. The detection system monitors the vertical position of the tip to construct a 3D map of the specimen. The tip radius, typically several nanometres, limits the lateral resolution of the map. Conventional AFMs have a low imaging rate. For example a high resolution image (512 x 512 pixels) could take over 10 minutes to collect [14]- [22, 23, 24]. This speed limitation is due to the serial nature of data collection, the bandwidth of the detection system and the control feedback loop.

The contact-mode HS-AFM at the Interface Analysis Centre (University of Bristol) images with a scan rate thousands of times higher than a conventional AFM [25]. The topographic information is collected via a single point laser vibrometer, which measures the cantilever's vertical displacement just above the tip [25] as the specimen is oscillated in a sinusoidal raster scan pattern using a custom piezo flexure stage. This contact-mode setup enables the imaging of larger specimen areas compared to conventional intermittent-contact or contact-mode methods [26]. The HS-AFM uses standard contact-mode cantilevers (MSNL, Bruker, USA). Displacement data was captured and image construction performed in real time using custom software (Bristol Nanodynamics, UK).

The large and high resolution imaging capabilities of this HS-AFM have proven effective at providing rapid nano and micro characterisation of specimen surfaces [27, 28, 29]. The increased specimen throughput compared to conventional AFM enables measurements with far greater statistical confidence [30] while the high frame rate allows the specimen surface to be observed in real-time.

Results

Following the specimen preparation described by Warren et al. [15], the surface was imaged under a droplet of demineralised water. The mosaic shown in **Figure 7** was captured in 10 seconds, and represents an imaging resolution comparable to transmission electron microscopy (TEM). This allowed rapid identification of numerous sensitised grain boundaries within ~50 μm of the specimen surface. Precipitates (~300 nm long) were evident at some grain boundaries, although precipitate-free grain boundaries were also scanned. The grain boundaries were ~100 nm wide. Previous TEM studies [31] have shown that the precipitates are Cr-carbides and that Cr depletion in the vicinity of the precipitates and in precipitate-free grain boundaries reaches levels below 10%.
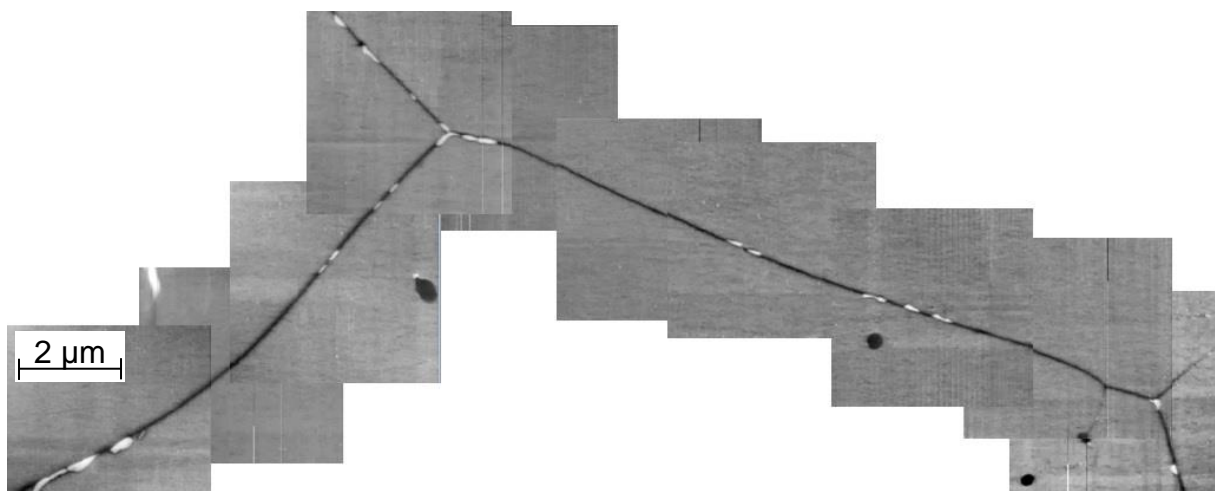

Figure 7: Mosaic of HS-AFM scans showing microstructure of a thermally sensitised 20Cr-25Ni-Nb stabilised stainless steel specimen (c-ring) cross section.

The aim of the experiment was to scan the surface in the first stages of corrosion initiation. However, even with chloride additions up to 1000 mg L^{-1} or after polarising the specimen in pure water up to +500 mV against a platinum pseudo-reference electrode, corrosion did not initiate during the experiment. In this short timescales, the microstructure was not affected by polarisation in the absence of chloride, or by chloride without external polarisation. The surface was then scanned under a droplet of demineralised water with 5 mg L^{-1} chloride, while simultaneously applying a potential of +500 mV. Within seconds, a large fraction of the grain boundary precipitates disappeared (**Figure 8**). The scale, 25 nm, in this figure relates to the z-range (black to white). It is expected that the Cr depletion at the grain boundaries of these thermally sensitised specimens may not be below the required 10% [31], given the need to undertake external polarisation.
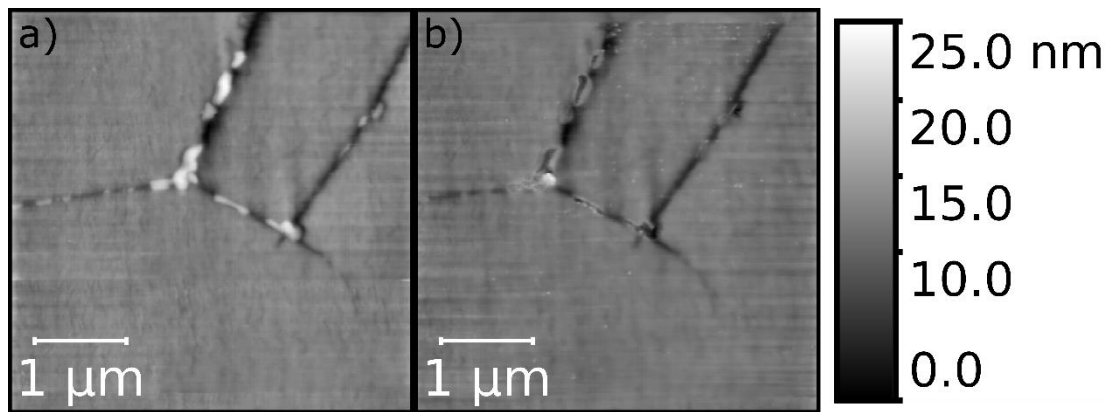
Figure 8: HS-AFM frames showing grain boundaries in sensitised stainless steel under a droplet of deionised water with 5 mg L^{-1} Cl$^-$: (a) before, and (b) after polarisation. Each 1-megapixel was collected in 0.5 s.

During corrosion initiation, most of the precipitates were replaced by voids or micro-pits. It is expected that the area adjacent to the grain boundary precipitates (thought to be Cr-carbides) will be heavily Cr-depleted. Once the depleted area is oxidised, the precipitates may then become detached from the microstructure. The change occurred rapidly, over a period of a few seconds, and was widespread across the surface. The imaging resolution was temporarily degraded when the precipitates were removed, although recovered quickly afterwards allowing imaging of the initiation sites. Indeed, corrosion products arising from the surface initiation sites interacted with the cantilever tip but subsequently dispersed into the bulk electrolyte.

A discontinuous chain of voids is formed along the grain boundary and voids at triple points are slightly larger due to the high concentration of precipitates in those regions. These voids may then become the initiation point for stress corrosion cracks to subsequently form. Characterisation of large areas of the surface showed that this had not occurred only in the area being characterised, and hence was not a result of the action of the AFM cantilever on the surface. However, not all precipitates were replaced by voids, and grain boundaries without precipitates were left intact after polarisation in a chloride environment. Those intact grain boundaries could have a different misorientation compared to the attacked grain boundary, and further analysis by electron back-scattered diffraction in a scanning electron microscope is being considered.
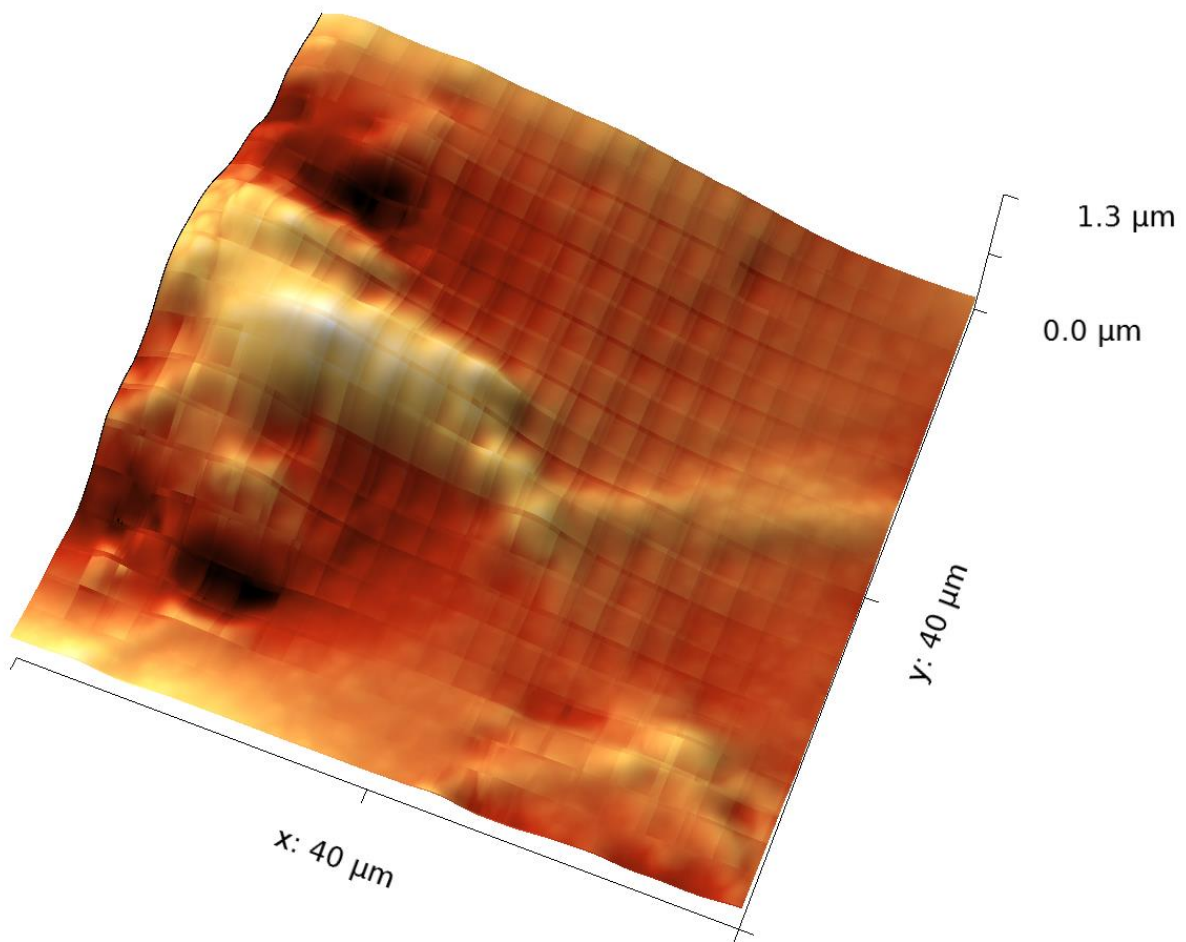
Figure 9: A composite HS-AFM topography map of a Magnox alloy specimen. The 50 mega-pixel image was collected in 100 s. The z-range in the figure is 1.3 μm.

The Magnox specimen was imaged post-corrosion using the same set-up as with the 20Cr-25Ni-Nb stabilised stainless steel. **Figure 9** shows a composite HS-AFM image collected over an area displaying filiform-like corrosion. The z-range in this figure (black to white) is 1.3 μm. The topography map shows a filament of corrosion product running left to right, away from a large pit, with dimensions too deep to image using this technique on the left of the frame. The filament measures between 3 μm and 12 μm wide, although much wider filament structures were observed optically on the same specimen. Large area mapping of areas with nanometre resolution can be used to map post-corrosion surfaces without biasing towards larger optically visible structures.

Conclusions

- 20Cr-25Ni-Nb stabilised stainless steel was thermally sensitised to artificially simulate Cr-depletion which occurs when irradiated in service.
- Novel HS-AFM was used to image the microstructure of both Magnox and AGR fuel cladding, with resolution comparable to TEM. It was also possible to scan a large area (hundreds of square micrometres) in extremely fast times. This demonstrates numerous possibilities for materials characterisation.
- HS-AFM imaging quality was maintained with the presence of a droplet of liquid on the specimen surface, enabling *in-situ* corrosion studies of 20Cr-25Ni-Nb.
- Corrosion was initiated by polarising the specimen whilst imaging in parallel using *in-situ* HS-AFM. It was found that the precipitates disappeared within seconds of polarising the specimen, leaving voids/micropits at grain boundaries. Various opportunities for technique development were identified which could overcome the loss in image quality as the corrosion products and bubbling interacts with the HS-AFM cantilever.
- TLI showed FFC spread rapidly across the surface of the Magnox alloy specimen undergoing corrosion. SVET revealed electrochemical detail on the mechanism. The results showed the intense net anodic activity at the filament head, and a small net cathodic area behind the propagating FFC.
- Sensitised 20Cr-25Ni-Nb stainless steel was imaged using *in-situ* SVET. Post corrosion observation indicated the presence of IGC. The results from SVET demonstrate corrosion initiation at a highly sensitised region of the stainless steel surface, which propagated under the haematite, correlating with micrographs taken following the experiment.

References

[1] B. Cox., "A new model for the in-reactor corrosion of zirconium alloys," IAEA, Vienna, 1997.

[2] A. T. Motta, A. Couet and R. J. Comstock, "Corrosion of zirconium alloys used for nuclear fuel cladding," *Annual review of materials research,* pp. 311-343, 2015.

[3] IAEA International working group on water reactor fuel performance and technology, "Fundemental aspects of corrosion on zirconium base alloys in water reactor environments," IAEA, 1990.

[4] B. Cox, "Some thoughts on the mechanisms of in-reactor corrosion of zirconium alloys," *Journal of nuclear materials,* vol. 336, pp. 331-368, 2005.

[5] D. I. R. Norris, C. Baker, C. Taylor and J. M. Titchmarsh, "Radiation-Induced Segregation in 20Cr/25Ni/Nb Stainless Steel," *15th Symposium on Effects of Radiation on Materials,* 1990.

[6] C. M. Chan, D. L. Engleberg and W. S. Walters, "Performance Characterisation of AGR Fuel Cladding Relevant to Long-Term in-Pond Storage in pH-moderated Aqeous Environment," in *Top Fuel Reactor Fuel Performance 2015*, Zurich, 2015.

[7] R. N. Clark, W. S. Walters and G. Williams, "A Scanning Probe Investigation of Intergranular Corrosion in Sensitised Stainless Steel Nuclear Fuel Cladding," in *NACE CORROSION 2016 Extended Abstracts*, Vancouver, 2016.

[8] C. H. Phuah, "Corrosion of Thermally-Aged Advanced Gas Reactor Fuel Cladding," Imperial College London Thesis, 2012.

[9] A. Al-Shater, D. Engleburg, S. Lyon, C. Donohoe, W. Walters, G. Whillock and A. Sherry, "Characterization of the Stress Corrosion Cracking Behavior of Thermally Sensitized 20Cr-25Ni Stainless Steel in a Simulated Cooling Pond Environment," *Journal of Nuclear Science and Technology,* pp. 1-10, 2017.

[10] M. Morozov, S. G. Pierce, G. Dobie, G. T. Bolton and T. Bennett, "Robotic Ultrasonic Testing of AGR Fuel Cladding," *Case Studies in Nondestructive Testing and Evaluation,* vol. 6, pp. 26-31, 2016.

[11] R. Burrows, S. Harris and N. P. C. Stevens, "Corrosion Electrochemistry of Fuel Element Materials in Pond Storage Conditions," *Trans. IChemE, Pt A, Chemical Engineering Research and Design,* vol. 83, no. A7, pp. 887-892, 2005.

[12] G. Williams, N. Birbilis and H. N. McMurray, "Controlling factors in localised corrosion morphologies observed for magnesium immersed in chloride containing electrolyte," *Faraday Discussions,* vol. 180, pp. 313-330, 2015.

[13] H. Godfrey and G. Cann, "Effect of Chloride on Magnox Corrosion with Respect to Carbon-14 Release Post Closure," National Nuclear Laboratory, NNL (14) 13189, 2016.

[14] O. Payton, L. Picco and T. B. Scott, "High speed atomic force microscopy for materials science," *Int. Mater. Rev.,* pp. 1-22, 2016.

[15] A. Warren, A. Martinez-Ubeda, O. Payton and L. Picco, "Preparation of stainless steel surfaces for scanning probe microscopy," *Micros. today,* vol. 24, 2016.

[16] International Atomic Energy Agency, "Further Analysis of Extended Storage of Spent Fuel," International Atomic Energy Agency, IAEA-TECDOC-944, 1997.

[17] G. Williams, H. A. L. Dafydd and R. Grace, "The localised corrosion of Mg alloy AZ31 in chloride containingelectrolyte studied by a scanning vibrating electrode technique," *Electrochimica Acta,* vol. 109, pp. 489-501, 2013.

[18] G. Williams and H. N. McMurray, "Localised corrosion of magnesium in chloride-containing electrolyte studied by a scanning vibrating electrode technique," *J. Electrochem Soc.,* vol. 155, no. 7, pp. C340-C349, 2008.

[19] G. Williams and H. N. McMurray, "Pitting corrosion of steam turbine blading steels: The influence of chromium content, temperature, and chloride ion concentration," *Corrosion,* vol. 62, no. 3, pp. 231-242, 2006.

[20] G. Williams, N. Birbilis and H. N. McMurray, "The Source of Hydrogen Evolved From a Magnesium Anode," *Electrochemistry Communications,* vol. 36, pp. 1-5, 2013.

[21] G. Williams and R. Grace, "Chloride-induced Filiform Corrosion of Organic Coated Magnesium," *Electrochimica Acta,* vol. 56, no. 4, pp. 189-1903, 2011.

[22] S. Hosaka, K. Etoh, A. Kikukawa and H. Koyanagi, "Megahertz silicon atomic force microscopy (AFM) cantilever and high-speed readout in AFM-based recording," *J. Vac. Sci. Technol. B Microelectron. Nanom. Struct.,* vol. 18, no. 1, pp. 94-99, 2000.

[23] G. T. Paloczi, B. L. Smith, P. K. Hansma, D. A. Walters and M. A. Wendmen, "Rapid imaging of calcite crystal growth using atomic force microscopy with small cantilevers," *Appl. Phys. lett.,* vol. 73, no. 12, pp. 1658-1660, 1998.

[24] T. Ando. , "High-speed atomic force microscopy coming of age," *Nanotechnology,* vol. 23, no. 6, pp. 62001-27, 2012.

[25] O. D. Payton, L. Picco, D. Robert, A. Raman, M. E. Homer, A. R. Champneys and M. J. Miles, "High-speed atomic force microscopy in slow motion - Understanding cantilever behaviour at high scan velocities," *Nanotechnology,* vol. 23, no. 20, p. 205704, 2012.

[26] O. D. Payton, L. Picco and T. B. Scott, "High-speed atomic force microscopy for materials science," *International Materials Reviews,* vol. 61, no. 8, pp. 473-494, 2016.

[27] A. M. Adamska, E. L. Bright, J. Sutcliffe, W. Liu, O. D. Payton and T. B. Scott, "Characterisation of electrodeposited polycrystalline uranium dioxide thin films on nickel foil for industrial applications," *Thin solid films,* vol. 597, pp. 57-64, 2015.

[28] A. M. Adamska, R. Springell, A. D. Warren, L. Picco, O. D. Payton and T. B. Scott, "Growth and characterisation of uranium-zirconum alloy films for nuclear industry applications," *J. Phys,* vol. 47, no. 31, pp. 301-315, 2014.

[29] A. J. Popel, A. M. Adamska, P. G. Martin , O. D. Payton, G. I. Lampronti, L. Picco, R. Springell, T. B. Scott, I. Monnet, C. Grygiel and I. Farnan, "Structural effects in UO2 thin films irradiated with U ions," *Nucl. Instruments Mathods Phys. Res. Sect. B Beam Interact. with Mater. Atoms,* vol. 386, pp. 8-15, 2016.

[30] P. L. Cullen, K. M. Cox, M. K. Bin Subhan, L. Picco, O. D. Payton, D. J. Buckley, T. S. Miller, S. A. Hodge, N. T. Skipper, V. Tileli and C. A. Howard, "Ionic solutions of two-dimensional materials," *Nat. Chem.,* 2016.

[31] C. J. Moss and J. M. Sykes, "Thermal Sensitisation of 20Cr/25Ni/Nb Stainless Steel," *Symposium on Radiation-Induced Sensitization of Stainless Steels,* 1986.